Journal of Enhanced Heat Transfer, 27(4):367–387 (2020)

HEAT TRANSFER ENHANCEMENT CAUSED BY IMPINGING JETS OF Al_2O_3–WATER NANOFLUID ON A MICRO-PIN FIN ROUGHENED SURFACE UNDER CROSSFLOW CONDITIONS—A NUMERICAL STUDY

Usman Allauddin,[1,*] Tariq Jamil,[1] Muhammad Shakaib,[1] H.M. Usman Khan,[1] Rafay Mohiuddin,[1] M. Saad Saeed,[1] Haseeb Ahsan,[1] & Naseem Uddin[2]

[1]*Mechanical Engineering Department, NEDUET, Karachi 75270, Pakistan*

[2]*Universiti Teknologi Brunei, Gadong BE1410, Brunei Darussalam*

*Address all correspondence to: Usman Allauddin, Mechanical Engineering Department, NEDUET, Karachi 75270, Pakistan; Tel.: +92 21 9926 1261; Fax: +92 21 9926 1255, E-mail: usman.allauddin@neduet.edu.pk

Original Manuscript Submitted: 12/27/2019; Final Draft Received: 5/8/2020

Advanced electronic devices need ultrahigh performance cooling techniques. One such technique is jet impingement cooling. This study numerically investigates the thermal performance and flow behavior of an array of alumina oxide–water nanofluid impinging jet systems under crossflow. The Reynolds number of the jet array ranges between 4000 and 20,000 with a normalized distance between the jet's outlet and target plate (Z/D) equal to 3. The target wall is roughened with micro-pin fins for surface enlargement. All of the computations are done in ANSYS-FLUENT using the shear stress transport k-ω turbulence model. The paper reports numerical predictions matching satisfactorily well with the empirical data. However, more research in the context of turbulence models solely for turbulent nanofluid modeling is recommended for future studies. The influence of volumetric concentrations $\phi = 0\%$, 0.2%, 0.7%, 1.5%, and 3% of Al_2O_3 nanoparticles is explored. It is inferred from the simulations that the addition of the nanoparticles does not influence the velocity field with the simplified method used in the current work. It can also be inferred that the increasing values of the nanoparticle concentration would cause a rise in the nanofluid equivalent thermal conductivity leading to a reduction in the Nusselt number, whereas the average convective heat transfer coefficient would improve. About 72% improvement in the heat transfer coefficient (h) of the nanofluid is observed while the Nusselt number is reduced by about 30% at volumetric concentration $\phi = 3\%$. The addition of pin fins would help in further heat transfer improvement.

KEY WORDS: *multiple impinging jets, Al_2O_3–water nanofluid, confined jet, surface enlargement, micro-pin fins*

NOMENCLATURE

A	area of the target plate	Z	distance between jet's outlet and the target plate (duct and rib dimension)
c	width of pin (duct and rib dimension)		
C_p	specific heat		
D	jet diameter		
Ext.	extended surface of the domain	z	coordinate perpendicular to the target wall
GCI	grid convergence index	z^+	dimensionless distance normal to target wall
H	convection heat transfer coefficient		
h	height of pin (duct and rib dimension)	**Greek Symbols**	
k	turbulent kinetic energy	ϑ	kinematic viscosity
Nu	Nusselt number	λ	thermal conductivity
p	pitch between pins (duct and rib dimension)	μ	absolute viscosity
		ρ	density
Pr	Prandtl number	ϕ	volumetric concentration
$\dot{Q}$	heat flux	ω	specific dissipation rate
Re	Reynolds number	**Subscripts**	
S	spacing between jets (duct and rib dimension)	avg	projected area averaged
		b	base fluid
T	jet temperature	j	inlet jet
V	jet velocity at the inlet	n	nanoparticle
X	streamwise distance (duct and rib dimension)	nf	nanofluid
		t	turbulent
Y	spanwise distance (duct and rib dimension)	w	target plate
		w,avg	effective area averaged

1. INTRODUCTION

Practical systems using impinging jet–based cooling/heating is one of the effective heat transfer methodologies typically used for significant heat removal from electronic chips, gas turbine blades, metal components, etc. Although the technique is quite old and well established, it is still an area of intense research for additional augmentation in the thermal performance of the impinging jet. There are several proven approaches for such improvements. This paper is focused on two approaches, namely, surface enlargement and thermophysical property alterations of the base fluid. Guo (2019) provided a review of heat transfer enhancement studies carried out in 2018. It has been reported that out of about 17,000 articles published in 2018, about 4600 articles were related to heat transfer enhancement. This shows the level of active research being conducted in the area of heat transfer enhancement.

The overall performance of an impinging jet system depends on factors such as the jet's Reynolds number (Re), geometry of the nozzle, nozzle diameter (D), distance between the jet's outlet and the target wall (Z), target surface, etc. Zuckerman and Lior (2006) discussed different parameters affecting the performance of jet impingement systems. They also reviewed applications, different empirical correlations, and numerical techniques used to model impinging jets. The pros and cons of different modeling techniques of turbulent jet impingement systems are also discussed in this paper.

The impingement of multiple jets is used in a variety of industrial applications. Single jet impingement flow is itself highly complex. The interaction between different jets of the array of a jet impingement system and the presence of crossflow, along with the axial flow, make multiple impinging jets extremely complex. Zuckerman and Lior (2006), Martin (1977), and Weigand and Spring (2009) have provided detailed reviews describing different parameters affecting the performance of the array of jet impingement systems. Xing et al. (2010) experimentally inspected different configurations of multiple impinging jets with air as the working fluid over a flat plate. The influence of the distance between the jet and target wall and the Reynolds number was investigated under different crossflow configurations by using $Z/D = 3$, 4, and 5 and Re = 15,000, 25,000, and 35,000. Xing et al. (2010) reported that high Re and lower Z/D values with an inline arrangement of jet arrays give the best heat transfer performance. They also showed that numerical techniques have the potential to give results closer to the experimentally measured ones. Caliskan et al. (2014) experimentally studied circular, rectangular, and elliptical nozzle geometries with different aspect ratios (0.5, 1, and 2) in an array of impinging jets. It was found that the elliptical-shaped nozzle provided greater heat transfer than the rectangular and circular nozzle exit geometries. The increasing values of the aspect ratio brought a rise in thermal performance. The heat transfer coefficient improved about 6%–16.8% depending on different combinations of the impinging jets. A numerical analysis was also done to support the experimental findings and to understand the flow structures.

The thermal characteristics of impinging jet systems can be enhanced by surface roughening of the target plate. Ribs, fins, dimples, etc., are commonly used as surface enlargement elements. They increase the heat transfer area and also induce flow structures of different length scales that ultimately affect the turbulence of the flow. A number of scientists have investigated improving the performance of impinging jet systems by using the aforementioned method. Spring et al. (2012), in a combined experimental and numerical study, compared inline and staggered arrangements of ribs. The thermal performance was found to be better with a staggered arrangement of ribs. These authors emphasized that a wetted surface area should be considered when comparing the heat flux with and without surface enlargement elements. Xing et al. (2011) used micro-ribs as surface enlargement elements and investigated the ribs' effects at Reynolds numbers Re = 15,000, 25,000, and 35,000 and normalized distance between the jet's outlet and the target wall at $Z/D = 3$, 4, and 5. The distance $Z/D = 3$ gave the best heat transfer results. Furthermore, micro-ribs were found to give better thermal performance than the flat target wall in all cases. These authors also concluded that numerical techniques can be used to complement experimental results, especially in rib-roughened impinging jet cases. The heat transfer characteristics of a micro-W–shaped roughened target plate were studied at Reynolds numbers in the range of 15,000–30,000 by Rao et al. (2016). Up to 9.6% improvement in the area-averaged heat transfer with negligible pressure drop was observed. Wan et al. (2015) performed numerical investigations using a cubical pin-fin roughened target plate within multiple impinging jets with different rib arrangements at $Z/D = 3.0$. They observed about 34.5% improvement in the thermal performance in comparison to the flat plate with a 3% decrease in the discharge coefficient.

Brakmann et al. (2015) studied the impact of a square micro-pin roughened target plate on the thermal performance and pressure losses within multiple impinging jets. The study was conducted at $Z/D = 3$–5 and Re = 15,000–35,000 with different crossflow configurations. The surface enlargers improved the effective surface area of the target plate by about 150% compared to the flat plate, causing about 142% enhancement in the heat flux. It was also found that the numerical study with the shear stress transport (SST) k-ω turbulence model gave predictions that agreed well those obtained with the experimental data. Lu et al. (2018) experimentally inspected the effects of the shape and height of micro-pin fins at Re = 2000–10,000 and $Z/D =$ 0.75–3. About 30%–120% improvement in the thermal performance compared to the flat target plate was observed with a similar discharge coefficient. The shape of the micro-pin fins exhibited no impact on the thermal performance.

Basic fluids such as water, oil, etc., which are commonly used in engineering applications, have low thermal conductivity. Thus, other than surface roughening through ribs, fins, etc., an appropriate method for thermal augmentation in impinging jet systems would be to modify the fluid properties by adding nanoparticles. The combination of nanosized particles and fluids yields a heat transfer medium with much better thermal conduction characteristics (Pourmehran et al., 2018). Numerous recently published research studies have investigated the impact of different nanoparticles on the performance of heat pipes, solar collectors, microchannels in heat sink devices, disc-type heaters with pool and convective boiling conditions, heat exchangers, nonconventional enclosures, and helically coiled tubes and annuli (Sarafraz et al., 2016, 2019; Sarafraz and Safaei, 2019; Sarafraz and Arjomandi, 2018; Nandakrishnan et al., 2018; Salari et al., 2015, 2017; Khanlari et al., 2019; Abbood et al., 2018; Fard et al., 2019; Fathian et al., 2020). Similarly, several review articles have discussed in detail the flow dynamics and effectiveness of heat exchangers, solar water heaters, and porous media with nanofluids (Guo, 2020; Molana, 2016; Mahian et al., 2013; Kasaeian et al., 2017). A few experimental and numerical studies in which nanofluid-based impinging jet systems were examined have also been carried out. Zeitoun and Ali (2012) conducted an experimental investigation to determine the thermal characteristics of an impinging jet with Al_2O_3–water nanofluid at volumetric concentrations of $\phi = 0\%$, 6.6%, and 10% over a horizontal circular disk. At the same Re value, improvement in the thermal performance was observed with increasing values of the concentration of nanoparticles. However, an increase in the size of the disk resulted in a decrease in the thermal performance. Barewar et al. (2019) performed an experimental study to investigate thermal enhancement with the inclusion of ZnO nanoparticles in a free surface water impinging jet over a heated copper plate. The experiments were performed at $\phi = 0.02\%$, 0.04%, 0.06%, and 0.1%; Re = 2192–9241; and $Z/D = 2$–7.5. About 51% improvement in the thermal performance was observed at $\phi =$ 0.1% and $Z/D = 3.5$. Naphon et al. (2018) carried out an experimental investigation to study the thermal performance of TiO_2–water nanofluid jet impingement over a microchannel heat sink. The work showed that convective heat transfer was improved with increasing nozzle diameter, decreasing distance between the jet's outlet and the target wall, and increasing concentration of nanoparticles. About 18.56% enhancement in convective heat transfer at $\phi = 0.015\%$ was observed.

Among numerical studies, Allauddin et al. (2018) performed numerical validation of the Zeitoun and Ali (2012) experimental work and observed numerical predictions very close to the experimental data. The numerically predicted local Nusselt (Nu) numbers were found to vary considerably with the Reynolds number. The proportional relation was shown to be $\mathrm{Nu} \propto \mathrm{Re}^{2/3}$. Lorenzo et al. (2012) investigated laminar slot jet impingement, in a confined configuration, with a mixture of water and Al_2O_3 nanoparticles. The bulk temperature of the nanofluid was increased

due to a rise in the effective thermal conductivity by the induction of nanoparticles. About 32% improvement in the thermal performance was observed at $\phi = 5\%$ and $Z/W = 8$ with pumping power about 3.9 times more than that of the base fluid. Senkal and Torii (2015) conducted a joint experimental and numerical investigation using air and Al_2O_3–water nanofluid. The nanofluid jet impingement showed greater heat transfer performance than the air impingement.

The current work presents a numerical study of a unique combination of multiple impinging jets, micro-pin fins, and nanofluids under crossflow conditions. Several researchers have shown that they all show improved heat transfer when used individually. To the best of the authors' knowledge, the available literature lacks investigations of the unique combination of a nanofluid with multiple impinging jets on a micro-pin fin roughened target plate. In the current work, the thermal performance and the fluid flow characteristics within an array of jets with water–Al_2O_3 nanofluid under maximum crossflow configuration over a micro-pin fin roughened target plate are investigated. Table 1 tabulates the different cases simulated in the current study.

2. GOVERNING EQUATIONS

The following set of transport equations is solved using a three-dimensional (3D) steady, incompressible Reynolds-averaged Navier–Stokes (RANS) method with the SST k-ω turbulence model proposed by Menter (1994):

$$\frac{\partial U_i}{\partial x_i} = 0 \tag{1}$$

$$\frac{\partial (\rho U_j U_i)}{\partial x_j} = -\frac{\partial P}{\partial x_i} + \frac{\partial}{\partial x_j}\left[\mu\left(\frac{\partial U_i}{\partial x_j} + \frac{\partial U_j}{\partial x_i}\right) - \rho\overline{U_i' U_j'}\right] \tag{2}$$

$$\frac{\partial (\rho U_i T)}{\partial x_i} = \frac{\partial}{\partial x_i}\left[k\frac{\partial T}{\partial x_i} - \rho C_p \overline{U_i' T'}\right] \tag{3}$$

where U_i represents the mean velocity component in the x_i direction; U_i' represents the fluctuating component of velocity U_i; T is the temperature; T' is the fluctuating component of T; P is the pressure; ρ is the fluid density; Pr denotes the Prandtl number; C_p represents the specific heat; and μ is the dynamic viscosity. In the current work, the modeling of the nanofluid

TABLE 1: Summary of different cases simulated in the current work

Number	Case	Description	Reynolds Number
1	Jet impingement with air on a smooth target plate (for model validation)	Impingement from multiple jets on a smooth target plate with air as the working fluid	4000; 10,000; 20,000
2	Jet impingement with air on a roughened target plate (for model validation)	Impingement from multiple jets on a micro-pin fin roughened target plate with air as the working fluid	4000; 10,000; 18,000
3	Jet impingement with nanofluid	Impingement from multiple jets on a micro-pin fin roughened target plate with nanofluid at $\phi = 0\%$–3%	4000; 10,000; 18,000

is done with the assumption that the nanofluid is considered to be a single-phase mixture. The thermophysical properties of the nanofluid are also assumed to be constant in this method. The single-phase assumption allows the governing equations of the pure fluid flow to be directly used for nanofluid modeling. The thermophysical properties are calculated with some empirical correlations. Kakac and Pramuanjaroenkij (2016) provided a review of around 100 numerical studies that used a single-phase modeling method for nanofluids. Several researchers have reported that the single-phase assumption is adequate for predicting different characteristics of nanofluid systems.

Different turbulence models are available in the commercial codes. Several researchers have reported very good accuracy with the comparatively low computational cost of the SST k-ω model for the impinging jet case (Caliskan et al., 2014; Spring et al., 2012; Xing et al., 2011; Rao et al., 2016; Wan et al., 2015; Brakmann et al., 2015; Zu et al., 2009). Peng et al. (2014) found accurate performance of the SST k-ω model in predicting the thermal characteristics of nanofluids in the jet impingement case. Recently, Allauddin et al. (2018) employed the SST k-ω model for numerical prediction of the thermal and velocity field characteristics of jet impingement cases on a flat surface with and without nanoparticles. The predictions made with the SST k-ω model were found to match very well with the validation data. Therefore, all of the simulations performed in the present study were executed with the SST k-ω turbulence model:

$$\frac{\partial k}{\partial t} + U_j \frac{\partial k}{\partial x_j} = P_k - \beta^* k\omega + \frac{\partial}{\partial x_j}\left[(\nu - \sigma_k \nu_t)\frac{\partial k}{\partial x_j}\right] \tag{4}$$

$$\frac{\partial \omega}{\partial t} + U_j \frac{\mathrm{d}\omega}{\partial x_j} = \alpha s^2 - \beta\omega^2 + \frac{\partial}{\partial x_j}\left[(\nu + \sigma_\omega \nu_t)\ \frac{\partial \omega}{\partial_i}\right] + 2\,(1-F)\,\sigma_{\omega 2}\frac{1}{\omega}\frac{\partial k}{\partial x_i}\frac{\partial \omega}{\partial x_i} \tag{5}$$

$$\nu_t = \frac{\alpha_1 k}{\max(\alpha, \omega, SF_2)} \tag{6}$$

2.1 Closure Coefficients and Auxiliary Relations

$$F_2 = \tanh\left\{\left[\max\left(\frac{2\sqrt{k}}{\beta^*\omega y}, \frac{500U}{y^2\omega}\right)\right]^2\right\} \tag{7}$$

$$P_k = \min\left(\tau_{ij}\frac{\partial v_i}{\partial x_j}, 10\beta^* k\omega\right) \tag{8}$$

$$F_1 = \tanh\left\{\min\left[\max\left(\frac{2\sqrt{k}}{\beta^*\omega y}, \frac{500U}{y^2\omega}\right)\frac{4\sigma_{\omega^2} k}{CD_{k\omega} y^2}\right]^4\right\} \tag{9}$$

$$CD_{k\omega} = \max\left(2\rho\sigma_{\omega 2}\frac{1}{\omega}\frac{\partial k}{\partial x_i}\frac{\partial \omega}{\partial x_i}, 10^{-10}\right) \tag{10}$$

$$\emptyset = \emptyset_1 F_1 + \emptyset_2\,(1 - F_1) \tag{11}$$

where $\alpha_1 = 5/9$, $\alpha_2 = 0.44$, $\beta_1 = 0.075$, $\beta_2 = 0.0828$, $\beta^* = 0.09$, $\alpha_{k1} = 0.85$, $\alpha_{k2} = 1$, $\alpha_{\omega 1}$ = 1.0, and $\alpha_{\omega 2} = 1/0.586$. With the single-phase assumption, Eq. (6) directly gives the turbulent eddy viscosity (ν_t) for the nanofluid as for the pure fluid.

3. THERMOPHYSICAL PROPERTIES OF THE NANOFLUID

The nanofluid was prepared by mixing highly conductive nanoparticles into base fluids such as water, ethylene glycol (EG), etc. In the current work, Al_2O_3 was used as the nanoparticles and water was utilized as the base fluid. The Al_2O_3–water nanofluid was modeled as an incompressible, Newtonian, single-phase fluid with constant thermophysical properties. The Al_2O_3–H_2O nanofluid, with a nanoparticle concentration of less than 10%, behaved as a Newtonian fluid in the temperature range of 0–90°C (Sahoo et al., 2009). The thermophysical properties of the alumina oxide nanoparticles and water (which was used as the base fluid) at 298 K are summarized in Table 2.

The correlation developed by Bhattacharya et al. (2004) was utilized to estimate the equivalent thermal conductivity of the nanofluid (λ_{nf}):

$$\lambda_{nf} = (1 - \phi)\,\lambda_b + \phi\lambda_n \tag{12}$$

where subscripts nf, b, and n represent the nanofluid, base fluid, and nanoparticles, respectively. The Brownian dynamics simulation technique coupled with the equilibrium Green–Kubo method was used to develop Eq. (12). The method showed that the predicted equivalent thermal conductivity values of the alumina–EG ($\phi = 0\%$–5%) and copper–EG (ϕ = 0%–0.6%) nanofluids agreed well with the experimental data. Jain et al. (2009) also used a similar technique to investigate the effect of various parameters on the equivalent thermal conductivity. Equation (12) was used to predict the λ_{nf} values for the volumetric concentration, particle size, and temperature, which ranged from 0.5% to 3%, 15 to 150 nm, and 290 to 320 K, respectively. The method showed that the predicted λ_{nf} values matched well with the experimental data.

The correlation established by Brinkman (1952) was utilized to calculate the equivalent viscosity of the nanofluid (μ_{nf}):

$$\mu_{nf} = \frac{\mu_f}{(1 - \phi)^{2.5}} \tag{13}$$

Equation (13) is valid for volumetric concentrations $\phi < 4\%$, as established from the pioneering Einstein formula $\mu_{nf} = \mu_f(1 + 2.5\phi)$. Brinkman's correlation has more acceptance than Einstein's formula, which is valid for low volumetric concentrations of $\phi < 0.02\%$ (Mahbubul et al., 2012).

The correlations developed by Pak and Cho (1998) were utilized to compute the equivalent density (ρ_{nf}) and specific heat ($C_{p_{nf}}$) of the nanofluid:

$$\rho_{nf} = (1 - \phi)\,\rho_f + \phi\rho_n \tag{14}$$

$$C_{p_{nf}} = (1 - \phi)\,C_{p_f} + \phi C_{p_n} \tag{15}$$

Equations (14) and (15) are a linear combination of the thermal conductivity/specific heat of the nanoparticles and base fluid. The correlations are based on the simple rule of mixtures proposed by Pak and Cho (1998). The properties of the nanofluid at different values of ϕ are summarized in Table 3.

TABLE 2: Thermophysical properties of Al_2O_3 and water

Fluid	ρ (kg/m^3)	λ (W/m·K)	μ (Pa·s)	C_p (J/kg·K)
Water	996.24	0.6158	0.0008206	4179
Al_2O_3 (Saini and Agarwal, 2016)	4000	30	—	880

TABLE 3: Thermophysical properties of Al_2O_3–water nanofluid for different values of volumetric concentration ϕ

ϕ (%)	ρ (kg/m^3)	λ (W/m·K)	μ (Pa·s)	C_p (J/kg·K)
0	996.24	0.6158	0.00082060	4179.0
0.2	1002.24	0.6747	0.00082470	4172.4
0.7	1017.30	0.8215	0.00083496	4158.9
1.5	1041.30	1.0560	0.00085137	4129.5
3	1086.40	1.4973	0.00088214	4080.0

4. COMPUTATIONAL DOMAIN AND BOUNDARY CONDITIONS

Figure 1 presents the computational domain employed in the current work along with the boundary conditions. Table 4 tabulates the dimensions of the computational domain. The computational time and effort are reduced by reducing the computational domain to a single row of eight jets by using the symmetry boundary condition in the spanwise direction. Figure 2 shows different views of the computational domain. The micro-pin fin roughened target plate can be seen in Fig. 2. At the inlet, the constant Dirichlet boundary condition for the velocity was applied with 5% turbulence intensity and a temperature of 298 K. The velocity was computed based on the Reynolds number of the corresponding case. The no-slip wall boundary condition with a fixed heat flux of 11,000 W/m^2 was used at the targeted wall. The outlet was modeled as the zero pressure gradient boundary condition with atmospheric-gauge pressure. The other end of the channel (opposite to the outlet) was modeled with the no-slip adiabatic wall boundary condition, which created the crossflow in the domain. The channel top wall excluding the jet's inlets was also modeled with the no-slip adiabatic wall boundary condition. The effect of the outlet

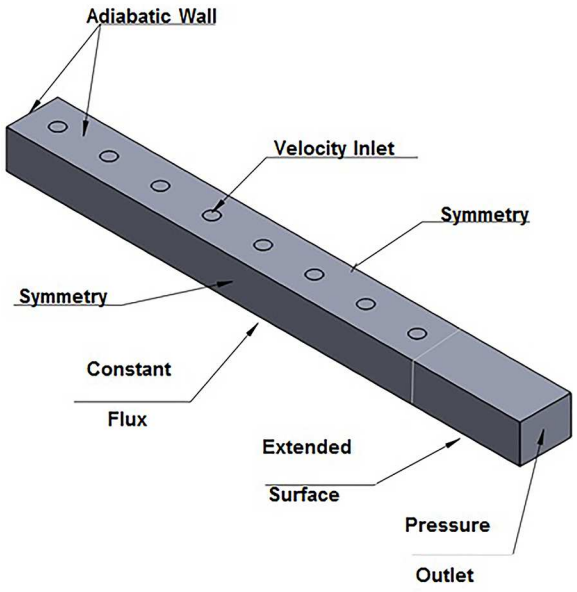

FIG. 1: Computational domain with all of the boundary conditions

TABLE 4: Dimensions of the computational domain

Parameter	Value (mm)
Jet diameter, D	4
Jet-to-jet spacing, S	20
Jet-to-plate spacing, Z	12
Pin side length, c	0.4
Pin height, h	0.8
Pin-to-pin spacing, p	1.2
Targeted impinging plate length	300

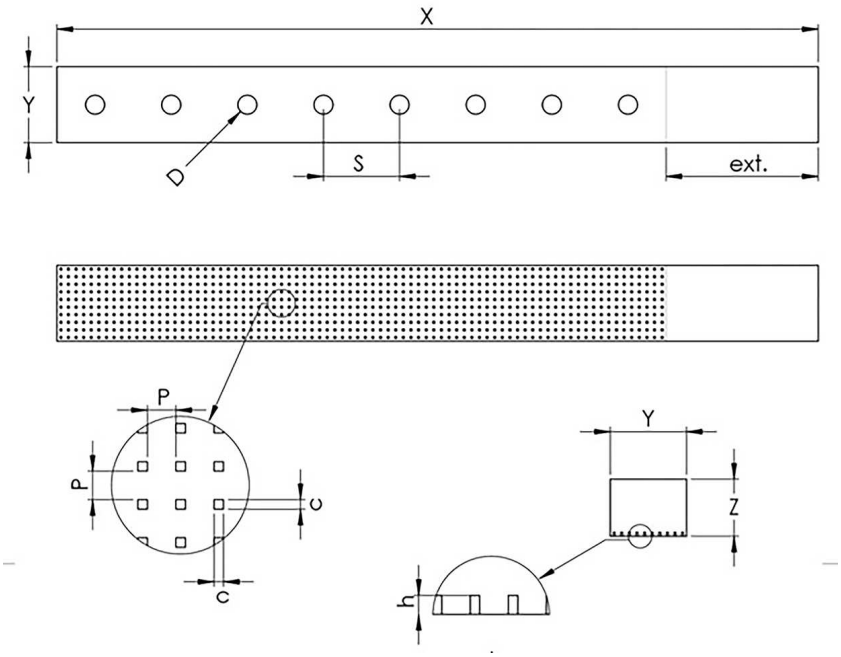

FIG. 2: Different views of the computational domain

boundary conditions at the impingement and jet flow regions was reduced by moving the outlet $8D$ away from the last impinging jet. The extended region reduced the divergence problems and also eliminated the effects of the outlet conditions at the main flow. The residual limit was set to be 10^{-6} as the convergence criterion for the continuity, momentum, energy, and turbulence model's equations.

5. NUMERICAL SETUP

The ANSYS Fluent computational fluid dynamics commercial package was used to carry out a 3D steady, incompressible study with the RANS method. The thermal and velocity fields were numerically predicted for the cases of multiple impinging jets of air, water, and Al_2O_3–water nanofluid with micro-pin fins as the surface enlargement element. The pressure-based solver

without body forces was used. All of the governing equations were discretized with the second-order upwind discretization scheme. Pressure velocity coupling was done using the semi-implicit method for pressure-linked equations algorithm. The wall effects were modeled using a low Reynolds number technique in which the near wall z^+ value is set as less than one. The turbulence modeling was done using the SST k-ω model. The SST model uses the k-ω turbulence model inside the boundary layer in the low Reynolds number region and switches to the k-ε turbulence model in the free-stream region. As elaborated in Section 2, the SST k-ω model predicts the thermal and velocity fields in jet impingement systems quite well.

The impinging jet Reynolds number is calculated as follows:

$$\mathrm{Re} = \frac{\rho V D}{\mu} \tag{16}$$

where V and D represent the jet inlet velocity and jet diameter, respectively. The projected area–averaged Nusselt number ($\mathrm{Nu}_{\mathrm{avg}}$) is calculated as follows:

$$\mathrm{Nu}_{\mathrm{avg}} = \frac{\dot{Q}}{A\,(T_w - T_j)} \cdot \frac{D}{\lambda} \tag{17}$$

while the effective area–averaged Nusselt number ($\mathrm{Nu}_{w,\mathrm{avg}}$) is calculated as follows:

$$\mathrm{Nu}_{w,\mathrm{avg}} = \frac{\dot{Q}}{A_{w,\mathrm{avg}}}(T_w - T_j) \cdot \frac{D}{\lambda} \tag{18}$$

where $\dot{Q}$ is the total heating power supplied to the target plate; D is the jet diameter; T_w is the temperature of the target plate; T_j is the jet inlet temperature; λ is the thermal conductivity of the fluid at the jet inlet temperature; A is the total projected area of the target plate; and $A_{w,\mathrm{avg}}$ is the effective area of the target plate with the surface enlargement elements. This same parameter ($\mathrm{Nu}_{w,\mathrm{avg}}$) is referred to as the wetted area–averaged Nusselt number in Wan et al. (2015). This definition of the Nusselt number represents the zone on the target wall influenced thermally by the incoming jet.

6. GRID INDEPENDENCE STUDY

A computational grid with insufficient refinement can result in significant errors in numerical modeling. These errors are called discretization errors. The well-established grid independence study method based on the Roach (1997) work was used in the current study to reduce the discretization errors. The grid convergence index (GCI) method is based on the Richardson extrapolation technique. However, this method cannot account for errors caused by improper boundary conditions or modeling techniques. Three systematically refined unstructured grids with tetrahedral elements having a constant refinement ratio of 1.2 were made. For near-wall modeling, inflation layers were used on the target wall. The number of inflation layers used in the grids was 22 with prism elements and a growth rate of 1.2. The size of the first grid cell in the wall normal direction z^+ was set to be less than one for all of the grids. A schematic view of the fine grid is presented in Fig. 3. The grid refinement done at the target wall is also shown in Fig. 3. A grid convergence check was performed for the multiple impinging jets in the micro-pin fin roughened target plate case with air at Re = 18,000. The details of the grids and $\mathrm{Nu}_{w,\mathrm{avg}}$ obtained at these grids are summarized in Table 5. The GCI for the fine grid was found to be 1.77%, which shows

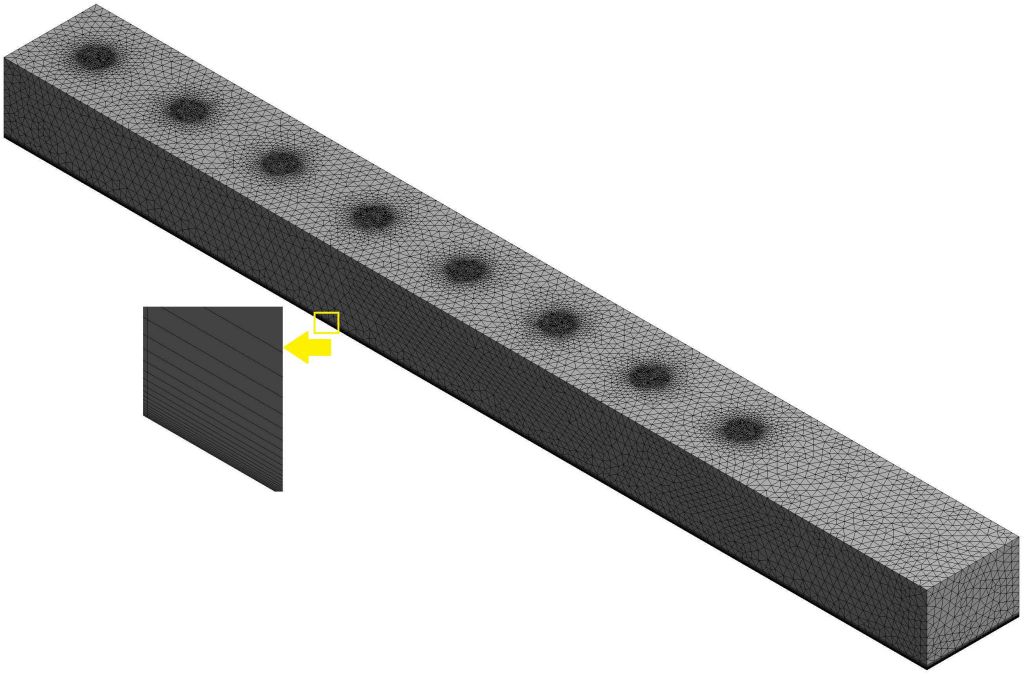

FIG. 3: Schematic view of the fine grid

TABLE 5: Summary of the grid Independence study at Re = 18,000

Case Number	Grid	Number of Elements (Millions)	z^+	$\mathbf{Nu}_{w,\mathbf{avg}}$
2	Coarse	2.94	0.22	66.46
	Medium	3.93	0.23	70.83
	Fine	5.34	0.26	72.31

that grid independence was achieved. Figure 4 presents a comparison of the centerline local Nu distributions with the three systematically refined grids, while Fig. 5 shows extrapolated GCI error bands. The GCI values were quite low, apart from some moderate peaks near the stagnation regions, suggesting that a mesh independent solution was achieved. Therefore, all of the other simulations in the paper were done on the fine grid.

The effect of the crossflow was at its maximum at the downstream end of the channel. The effect of the crossflow was observed from the second impinging jet and its magnitude started increasing toward the downstream end of the channel, as shown and further explained in Section 8.1. Flow acceleration was also observed in this region. It can be inferred that, due to the increased complex nature of the flow in the downstream region, differences were observed among the predictions made with the three grids when the normalized duct length X/D was 24–28, as shown in Fig. 4. Second, in the validation study, as shown and explained in the next section, it was observed that the numerical results were under-predicted. This under-prediction would be higher with coarse and medium grids since lower values of the Nusselt numbers were predicted in the X/D range of 24–28 compared to the fine mesh. Thus, it can be concluded that the fine grid gives more accurate results.

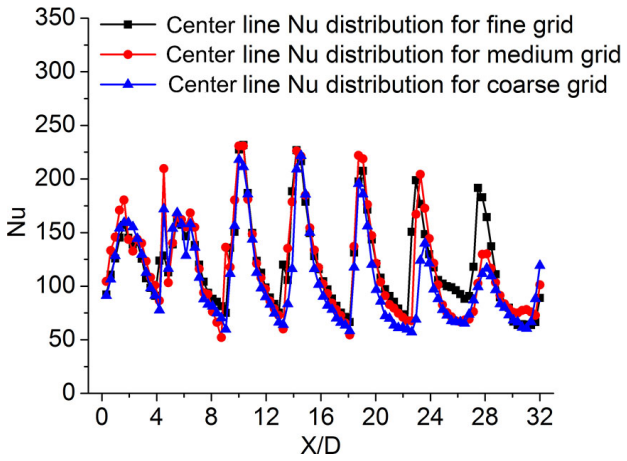

FIG. 4: Comparison of centerline Nusselt number distributions for different grids at Re = 18,000

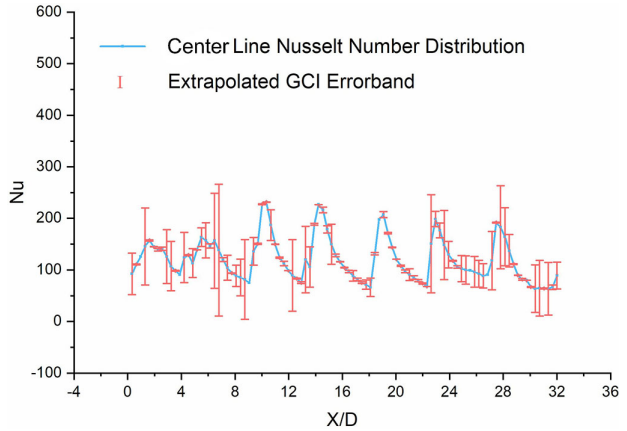

FIG. 5: GCI values along with the centerline Nusselt number distribution for the fine grid at Re = 18,000

7. MODEL VALIDATION

In the current work, the experimental database of Lu et al. (2018) was used to validate the numerical results. First, the case of multiple impinging air jets on a smooth target plate was simulated. The projected area–averaged Nusselt numbers were numerically predicted in the Reynolds number range of 4000 to 20,000 and validated with the corresponding experimental data. A comparison is presented in Fig. 6, were a very good match between the numerical predictions and the experimental data is observed. In general, the Nu value increased with increasing Re values. This trend was predicted well in the numerical simulations. Second, the Nu_{avg} values were calculated for the case of multiple impinging jets at Re = 4000, 10,000, and 18,000, where the target plate was roughened with micro-fins and air was the working fluid. A comparison of these values with the corresponding experimental data is given in Fig. 7, where it can be seen that the numerical values are generally under-predicted but the increasing trend of Nu_{avg} with increasing values of Re is captured very well. The deviation from the experimental data presented in Lu et al. (2018) was higher in the case of the target plate roughened with micro-fins compared to

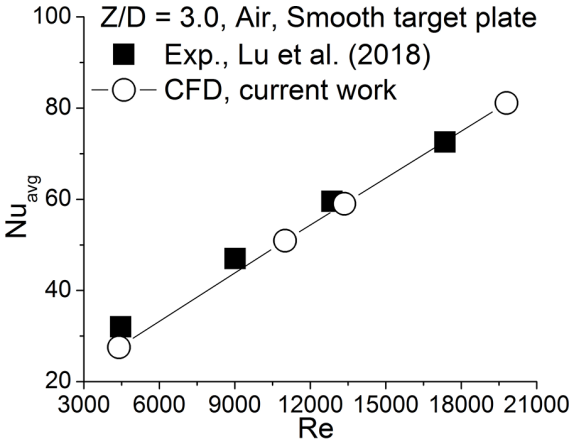

FIG. 6: Comparison between the numerically predicted values of the projected area–averaged Nusselt number and the experimental data of Lu et al. (2018) with air impingement on the smooth surface

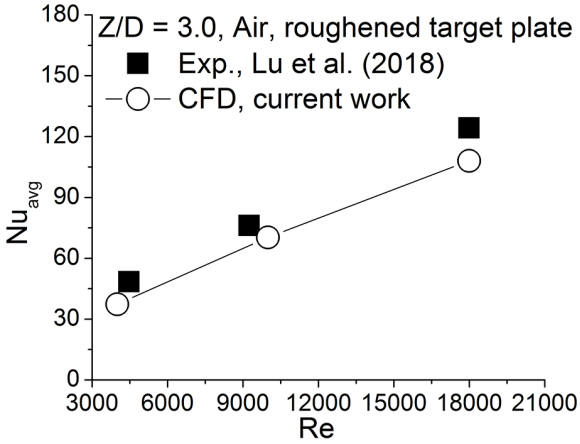

FIG. 7: Comparison between the numerically predicted values of the projected area–averaged Nusselt number and the experimental data of Lu et al. (2018) with air impingement on the roughened target plate

the smooth plate. Keeping in mind the complex nature of the flow due to the presence of the micro-pin fins, the errors between the numerical predictions and the experimental data can be considered acceptable.

A comparison between the projected area–averaged Nusselt number ($\mathrm{Nu}_{\mathrm{avg}}$) based on projected area A and the effective area–averaged Nusselt number ($\mathrm{Nu}_{w,\mathrm{avg}}$) based on effective area $A_{w,\mathrm{avg}}$ is shown in Fig. 8. The comaprison is shown for the case of multiple impinging jets on a target plate roughened with micro-fins having air as working fluid at Re = 4000, 10,000, and 18,000. The micro-pin fin roughened target plate had about 150% greater surface area than the flat plate. This enlargement of the surface area produced the high rates of heat transfer in the case of the micro-pin fin roughened target plate. It can be observed in Fig. 8 that the $\mathrm{Nu}_{w,\mathrm{avg}}$ values are much lower than the $\mathrm{Nu}_{\mathrm{avg}}$ values. This shows that the enhancement in thermal performance was mainly due to the amplification in the surface area of the target plate by the micro-pin fins.

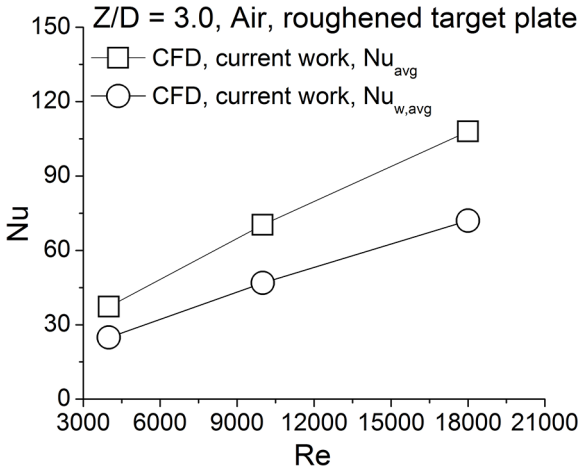

FIG. 8: Comparison between the numerical results of the projected area–averaged Nusselt number and the effective area–averaged Nusselt number with air impingement on the roughened target plate

The previous comparisons show the reliability of the current numerical model. The heat transfer results predicted by the current numerical model are in good agreement with the experimental data in the Re range of 4000–20,000. In the following sections, the performance of the impinging jet cases was investigated with the inclusion of Al_2O_3 nanoparticles using the same model. The study shows improvement in the heat transfer produced using nanoparticles along with surface enlargement of the target plate.

8. RESULTS AND DISCUSSION

In this section, the heat transfer and fluid flow characteristics of the target plate roughened with micro-pin fins and impinged with nanofluid will be discussed.

8.1 Flow Field

Figure 9 shows a comparison of the velocity field at different concentrations of nanoparticles for the case of the target plate roughened with micro-pin fins at Re = 18,000. The streamlines are also shown in Fig. 9. The comparison of the velocity field along with the streamlines is done on the central plane. The high-velocity regions are shown by the red color contours. The velocity distributions are not affected by the increasing ϕ values. All of the jets exhibit similar behavior, in that the axial flow velocities remain the same in the jet region. They strike the target plate, stagnation regions are formed, and the axial flow is converted into the wall jet flow. The vortex structures are also formed in the first four impinging jets near the stagnation regions. With the increasing distance from the second impinging jet, the impact of the crossflow can be observed, after which the impinging jets start to be deflected toward the downstream end of the channel. The flow is accelerated in the downstream end of the channel and the vortex structures are also removed. The increasing values of the volumetric coefficient increase the effective density and viscosity of the nanofluid, as shown in Table 3. The velocity at the jet inlet needs to be slightly decreased to keep the Re value constant, which can be observed in Fig. 9. For duct length $X/D < 12$, low-velocity regions including high-velocity impinging jets can be

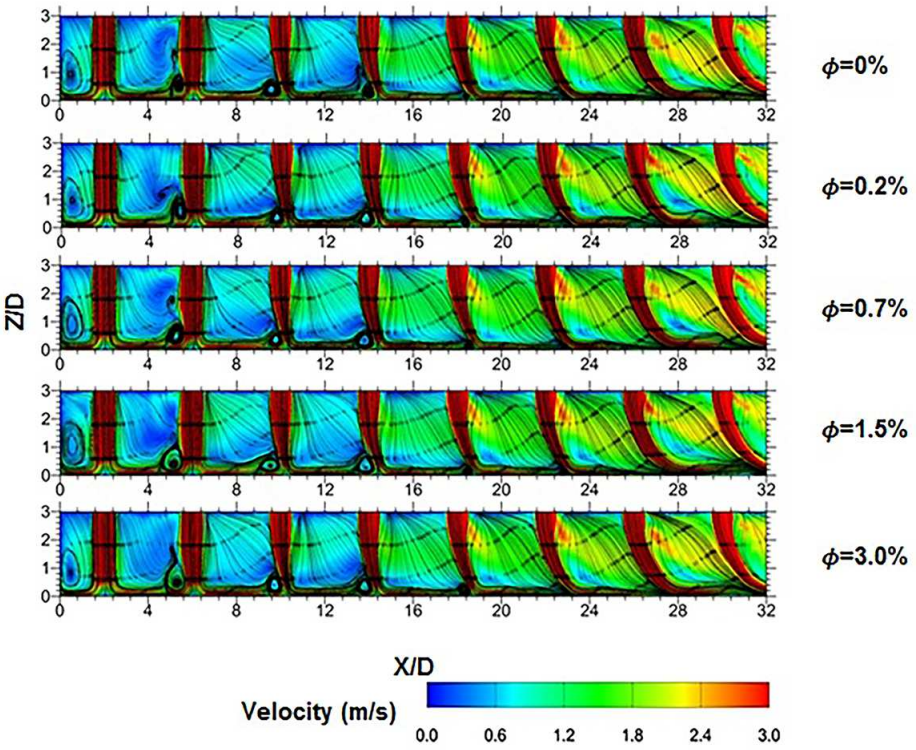

FIG. 9: Comparison between the velocity distributions on the longitudinal central plane for different concentrations of nanoparticles at Re = 18,000

observed. For $X/D > 12$, the effect of the crossflow starts to become visible and regions of high velocity can be observed to dominate the flow domain. These high-velocity regions show the flow acceleration produced due to the increasing effect of the crossflow with increasing distance in the downstream direction of the flow. The flow acceleration produced in the downstream region due to the crossflow also affects the heat transfer trends in these regions, which will be discussed in detail in the next section.

8.2 Heat Transfer

Figure 10 shows a comparison of the Nu_{avg} values for the case of multiple impinging jets with a micro-pin fin roughened target wall at different concentrations of nanoparticles ($\phi = 0\%$–3%) for Reynolds numbers ranging between 4000 and 18,000. An inverse relationship can be observed between Nu_{avg} and ϕ as the Nu_{avg} values decrease with an increase in the ϕ values. This behavior is due to the rise in the effective thermal conductivity of the nanofluid. The Nu value can be defined as the ratio between convective and conductive heat transfer. The high values of effective thermal conductivity eventually increase the conductive heat transfer, thus the Nu_{avg} value decreases as the ϕ values increase.

The effects of nanoparticles on the heat transfer coefficient and the target wall temperature were also determined. Figure 11 shows a comparison of the overall averaged heat transfer coefficient (h_{avg}) based on the projected area of the target plate for the case of multiple impinging

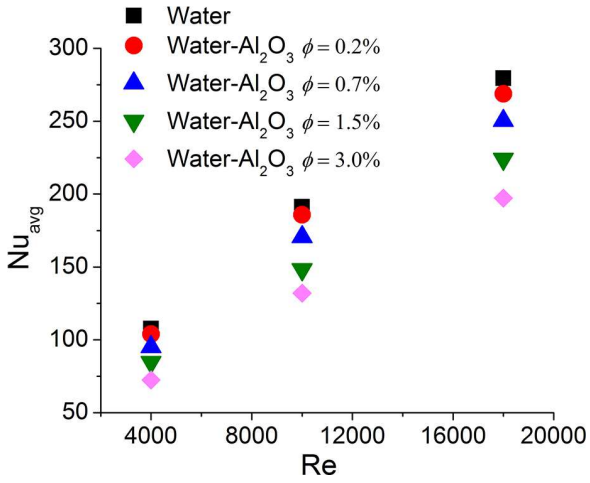

FIG. 10: Projected area–averaged Nusselt number over a micro-pin fin roughened target plate for different nanoparticle concentrations

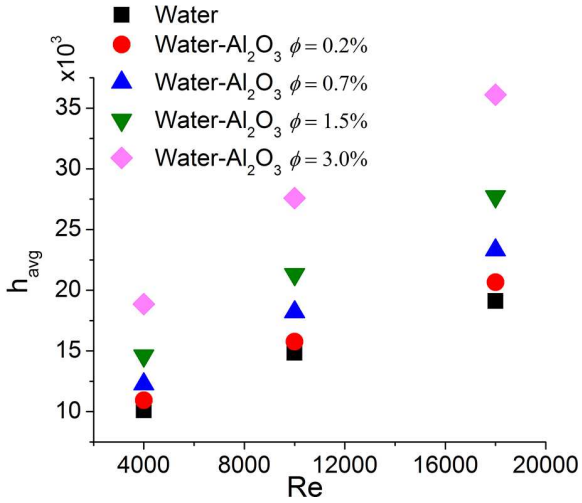

FIG. 11: Projected area–averaged heat transfer coefficients over the micro-pin fin roughened target plate for different nanoparticle concentrations

jets on a micro-pin fin roughened target plate at different concentrations of nanoparticles (ϕ = 0%–3%) for Reynolds numbers ranging between 4000 and 18,000. It can be observed that the averaged heat transfer coefficient values increase with increasing values of the volumetric concentration of nanoparticles at Reynolds numbers ranging from 4000 to 18,000. Table 6 shows a summary of the comparison between h_{nf}/h_b and $\mathrm{Nu}_{nf}/\mathrm{Nu}_b$ for different values of ϕ at Re = 18,000. About 72% enhancement in the heat transfer coefficient is observed at ϕ = 3%. In general, the h_{avg} values increase when the Reynolds number is increased with and without nanoparticles.

Figure 12 shows a comparison of the local Nu contours for the case of multiple impinging jets on a micro-pin fin roughened target plate at different concentrations of nanoparticles

TABLE 6: Comparison of area-averaged heat transfer characteristics of at Re = 18,000

ϕ (%)	h_{nf}/h_b	$\mathrm{Nu}_{nf}/\mathrm{Nu}_b$
0.2	1.05	0.962
0.7	1.19	0.895
1.5	1.37	0.801
3.0	1.72	0.705

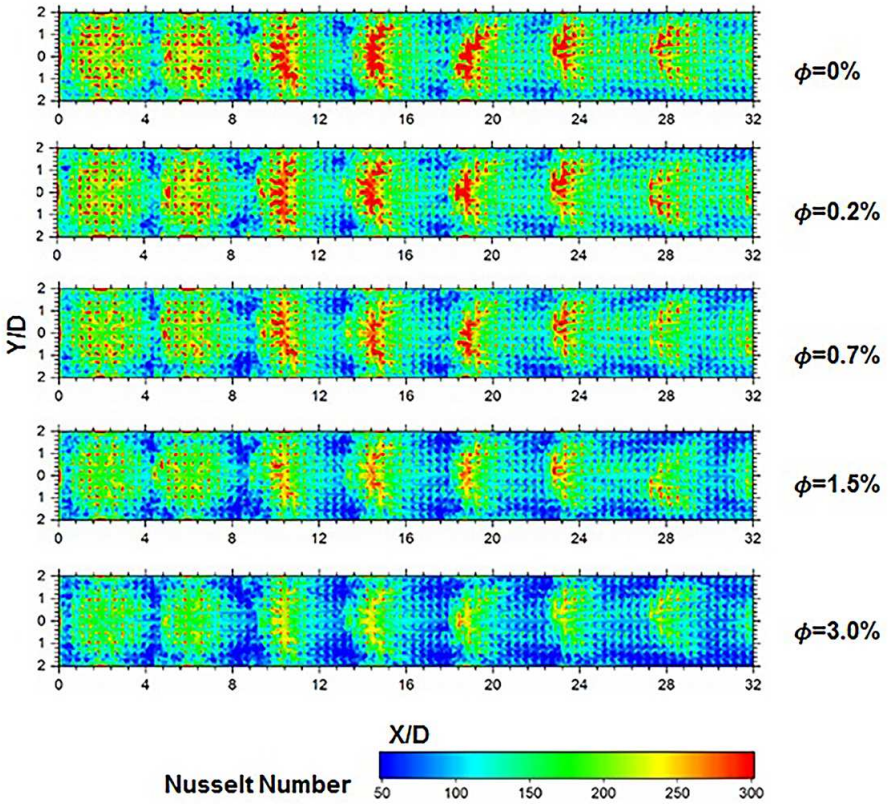

FIG. 12: Comparison between the local Nusselt number contours over the micro-pin fin roughened target plate for different nanoparticle concentrations at Re = 18,000

(ϕ = 0%–3%) for Reynolds number Re = 18,000. The local Nu contours of the target wall are shown. The red color contours show the high Nu values. In the stagnation region, the Nu values are significantly higher compared to the other regions. For the case of multiple impinging jets of pure water, the region having maximum Nu values is greater in size and is obtained in the middle portion of the channel. In the downstream end of the channel, the Nusselt number values decrease due to flow acceleration. The effects of the concentration of nanoparticles on the thermal field are also seen in Fig. 12. The local Nusselt number values decrease with increasing values of the concentration of nanoparticles. Figure 12 shows that the inclusion of fins would

be less effective if distance X/D is less than 8, since low values of the Nusselt number are observed. The high values of the Nusselt number are observed when the X/D ratio is between 10 and 24. In this X/D range, the maximum effect of impinging jet cooling is present. As X/D is further increased (i.e., $X/D > 24$), the Nusselt number values start to decrease due to the flow acceleration.

9. CONCLUSIONS

A numerical investigation was conducted to study the heat transfer enhancement and velocity field characteristics of a micro-pin fin roughened target plate with multiple impinging jets of Al_2O_3–water nanofluid. The values of Re = 4000–20,000, $\phi = 0\%$–3%, and $Z/D = 3$ under maximum crossflow conditions were used. The experimental data from Lu et al. (2018) was used to validate the numerical predictions of the current work. The following conclusions can be drawn from the present study:

1. It was observed that the simplified method of dealing with the nanofluid does not capture the real features of the velocity field of the nanofluids and the flow field is not affected by the addition of nanoparticles. However, since thermophysical properties were included in the simulations using the correlations, the heat transfer results were found to validate the experimental data. The current study is still useful in understanding the thermal augmentation resulting from the addition of nanoparticles.

2. The flow acceleration decreased the local Nu values on the impingement plate. The effect was further enhanced by an increase in the volumetric concentration of the nanoparticles, since this increased the conductive heat transfer. About 30% reduction in the Nu value was observed at volumetric concentration $\phi = 3\%$. An increment in the heat transfer coefficient values was observed with increasing values of the volumetric concentration of the nanoparticles. About 72% improvement in the heat transfer coefficient of the nanofluid was observed at volumetric concentration $\phi = 3\%$.

3. The modeling of the turbulent eddy viscosity was not vividly explored, and more research within the context of turbulence models solely for turbulent nanofluid modeling is needed in the future. The real effect of nanoparticles on the nanofluid flow field also needs to be investigated with more complex modeling techniques in future studies.

ACKNOWLEDGMENT

The first author is grateful to the Higher Education Commission of Pakistan for providing financial assistance under Start-Up Research Grant Program Project 2067.

REFERENCES

Abbood, S.A., Wang, J., Wu, Z., and Sunden, B., Analysis of Natural Convection of Cu and TiO_2 Nano-Fluids inside Nonconventional Enclosures, *J. Enhanced Heat Transf.*, vol. **25**, nos. 4-5, pp. 315–332, 2018.

Allauddin, U., Mahrukh, M., Rehman, N.U., Haque, M.E., and Uddin, N., Numerical Investigation of Heat Transfer by an Impinging Jet Using Alumina–Water Nanofluid, *Numer. Heat Transf.,. Part A: Appl.*, vol. **74**, no. 8, pp. 1486–1502, 2018.

Barewar, S.D., Tawri, S., and Chougule, S.S., Heat Transfer Characteristics of Free Nanofluid Impinging Jet on Flat Surface with Different Jet to Plate Distance: An Experimental Investigation, *Chem. Eng. Process. Process Intensif.*, vol. **136**, pp. 1–10, 2019.

Bhattacharya, P., Saha, S.K., Yadav, A., and Phelan, P.E., Brownian Dynamics Simulation to Determine the Effective Thermal Conductivity of Nano-Fluids, *J. Appl. Phys.*, vol. **95**, no. 11, pp. 6492–6494, 2004.

Brakmann, R., Chen, L., Weigand, B., and Crawford, M., Experimental and Numerical Heat Transfer Investigation of an Impinging Jet Array on a Target Plate Roughened by Cubic Micro Pin Fins, in *Proc. of ASME Turbo Expo 2015: Turbine Technical Conference and Exposition, Vol. 5A: Heat Transf.*, Montreal, QC, Canada, 2015.

Brinkman, H.C., The Viscosity of Concentrated Suspensions and Solutions, *J. Chem. Phys.*, vol. **20**, no. 4, p. 571, 1952.

Caliskan, S., Baskaya, S., and Calisir, T., Experimental and Numerical Investigation of Geometry Effects on Multiple Impinging Air Jets, *Int. J. Heat Mass Transf.*, vol. **75**, pp. 685–703, 2014.

Fard, A.M., Mirjalily, S.A.A., and Ahrar, A.J., Influence of Carbon Nanotubes on Pressure Drop and Heat Transfer Rate of Water in Helically Coiled Tubes, *J. Enhanced Heat Transf.*, vol. **26**, no. 3, pp. 217–233, 2019.

Fathian, F., Mirjalily, S.A.A., Salimpour, M.R., and Oloomi, S.A.A., Experimental Investigation of Convective Heat Transfer of Single and Multi-Walled Carbon Nanotubes/Water Flow inside Helical Annuli, *J. Enhanced Heat Transf.*, vol. **27**, no. 3, pp. 195–206, 2020.

Guo, Z., Heat Transfer Enhancement—A Brief Review of 2018 Literature, *J. Enhanced Heat Transf.*, vol. **26**, no. 5, pp. 429–449, 2019.

Guo, Z., A Review on Heat Transfer Enhancement with Nano-Fluids, *J. Enhanced Heat Transf.*, vol. **27**, no. 1, pp. 1–70, 2020.

Jain, S., Patel, H.E., and Das, S.K., Brownian Dynamics Simulation for the Prediction of Effective Thermal Conductivity of Nano-Fluid, *J. Nanoparticle Res.*, vol. **11**, no. 4, pp. 767–773, 2009.

Kakac, S. and Pramuanjaroenkij, A., Single-Phase and Two-Phase Treatments of Convective Heat Transfer Enhancement with Nano-Fluids—A State-of-the-Art Review, *Int. J. Therm. Sci.*, vol. **100**, pp. 75–97, 2016.

Kasaeian, A., Daneshazarian, R., Mahian, O., Kolsi, L., Chamkha, A.J., Wongwises, S., and Pop, I., Nanofluid Flow and Heat Transfer in Porous Media: A Review of the Latest Developments, *Int. J. Heat Mass Transf.*, vol. **107**, pp. 778–791, 2017.

Khanlari, A., Sözen, A., Variyenli, H.I., and Gürü, M., Comparison between Heat Transfer Characteristics of TiO_2/Deionized Water and Kaolin/Deionized Water Nano-Fluids in the Plate Heat Exchanger, *J. Enhanced Heat Transf.*, vol. **50**, no. 5, pp. 435–450, 2019.

Lorenzo, G.D., Manca, O., Nardini, S., and Ricci, D., Numerical Study of Laminar Confined Impinging Slot Jets with Nanofluids, *Adv. Mech. Eng.*, vol. **2012**, Article ID 248795, 2012. DOI: 10.1155/2012/248795

Lu, X., Li, W., Li, X., Ren, J., and Jiang, H., Influences of Micro Pin-Fin on Jet Array Impingement Heat Transfer: Effects of Jet to Target Distance, Micro Pin-Fin Shapes, Height, and Reynolds Number, in *Proc. of ASME Turbo Expo 2018: Turbomachinery Technical Conference and Exposition*, vol. **5A**, V05AT16A014, Oslo, Norway, 2018.

Mahbubul, I.M., Saidur, R., and Amalina, M.A., Latest Developments on the Viscosity of Nano-Fluids, *Int. J. Heat Mass Transf.*, vol. **55**, pp. 874–885, 2012.

Mahian, O., Kianifar, A., Kalogirou, S.A., Pop, I., and Wongwises, S., A Review of the Applications of Nanofluids in Solar Energy, *Int. J. Heat Mass Transf.*, vol. **57**, pp. 582–594, 2013.

Martin, H., Heat and Mass Transfer between Impinging Gas Jets and Solid Surfaces, *Adv. Heat Transf.*, vol. **13**, pp. 1–60, 1977.

Menter, F., Two-Equation Eddy-Viscosity Turbulence Models for Engineering Applications, *AIAA J.*, vol. **32**, no. 8, pp. 1598–1605, 1994.

Molana, M., A Comprehensive Review on the Nanofluids Application in the Tubular Heat Exchangers, *Am. J. Heat Mass Transf.*, vol. **3**, no. 5, pp. 352–381, 2016.

Nandakrishnan, S.L., Deepu, M., and Shine, S.R., Numerical Investigation of Heat-Transfer Enhancement in a Dimpled Diverging Microchannel with Al_2O_3–Water Nano-Fluid, *J. Enhanced Heat Transf.*, vol. **25**, nos. 4-5, pp. 347–365, 2018.

Naphon, P., Nakharintr, L., and Wiriyasart, S., Continuous Nanofluids Jet Impingement Heat Transfer and Flow in a Micro-Channel Heat Sink, *Int. J. Heat Mass Transf.*, vol. **126**, pp. 924–932, 2018.

Pak, B.C. and Cho, Y.I., Hydrodynamic and Heat Transfer Study of Dispersed Fluids with Submicron Metallic Oxide Particles, *Exp. Heat Transf.*, vol. **11**, no. 2, pp. 151–170, 1998.

Peng, W., Jizu, L., Minli, B., Yuyan, W., and Chengzhi, H., A Numerical Investigation of Impinging Jet Cooling with Nanofluids, *Nanoscale Microscale Thermophys. Eng.*, vol. **18**, no. 4, pp. 329–353, 2014.

Pourmehran, O., Sarafraz, M.M., Rahimi-Gorji, M., and Ganji, D.D., Rheological Behaviour of Various Metal-Based Nano-Fluids between Rotating Discs: A New Insight, *J. Taiwan Inst. Chem. E.*, vol. **88**, pp. 37–48, 2018.

Rao, Y., Chen, P., and Wan, C., Experimental and Numerical Investigation of Impingement Heat Transfer on the Surface with Micro W-Shaped Ribs, *Int. J. Heat Mass Transf.*, vol. **93**, pp. 683–694, 2016.

Roache, P.J., Quantification of Uncertainty in Computational Fluid Dynamics, *Annu. Rev. Fluid. Mech.*, vol. **29**, pp. 123–160, 1997.

Sahoo, B.C., Vajjha, R.S., Ganguli, R., Chukwu, G.A., and Das, D.K., Determination of Rheological Behavior of Aluminum Oxide Nanofluid and Development of New Viscosity Correlations, *Pet. Sci. Technol.*, vol. **27**, no. 15, pp. 1757–1770, 2009.

Saini, D. and Agarwal, G.D., Thermophysical Properties of Nano Fluids—A Review, *Int. J. Adv. Eng. Sci. Technol.*, vol. **5**, pp. 39–45, 2016.

Salari, E., Peyghambarzadeh, S.M., Sarafraz, M.M., and Hormozi, F., Boiling Thermal Performance of TiO_2 Aqueous NanoFluids as a Coolant on a Disc Copper Block, *Period. Polytech. Chem. Eng.*, vol. **60**, pp. 106–122, 2015.

Salari, E., Peyghambarzadeh, S.M., Sarafraz, M.M., Hormozi, F., and Nikkah, V., Thermal Behavior of Aqueous Iron Oxide Nano-Fluid as a Coolant on a Flat Disc Heater under the Pool Boiling Condition, *Heat Mass Transf.*, vol. **53**, pp. 265–275, 2017.

Sarafraz, M.M. and Arjomandi, M., Thermal Performance Analysis of a Microchannel Heat Sink Cooling with Copper Oxide–Indium (CuO/In) Nano-Suspensions at High-Temperatures, *Appl. Therm. Eng.*, vol. **137**, pp. 700–709, 2018.

Sarafraz, M.M., Arya, A. Nikkah, V., and Hormozi, F., Thermal Performance and Viscosity of Biologically Produced Silver/Coconut Oil Nanofluids, *Chem. Biochem. Eng. Q.*, vol. **30**, no. 4, pp. 489–500, 2016.

Sarafraz, M.M., Pourmehran, O., Yang, B., and Arjomandi, M., Assessment of the Thermal Performance of a Thermosyphon Heat Pipe Using Zirconia-Acetone Nanofluids, *Renewable Energy*, vol. **136**, pp. 884–895, 2019.

Sarafraz, M.M. and Safaei, M.R., Diurnal Thermal Evaluation of an Evacuated Tube Solar Collector (ETSC) Charged with Graphene Nanoplatelets-Methanol Nano-Suspension, *Renewable Energy*, vol. **142**, pp. 364–372, 2019.

Senkal, C. and Torii, S., Thermal Fluid Flow Transport Phenomena in Nanofluid Jet Array Impingement, *J. Flow Visual. Image Process.*, vol. **22**, pp. 59–79, 2015.

Spring, S., Xing, Y., and Weigand, B., An Experimental and Numerical Study of Heat Transfer from Arrays of Impinging Jets with Surface Ribs, *J. Heat Transf.*, vol. **134**, no. 8, p. 082201, 2012.

Wan, C., Rao, Y., and Chen, P., Numerical Predictions of Jet Impingement Heat Transfer on Square Pin-Fin Roughened Plates, *Appl. Therm. Eng.*, vol. **80**, pp. 301–309, 2015.

Weigand, B. and Spring, S., Multiple Jet Impingement—A Review, in *Proc. of International Symposium on Heat Transfer in Gas Turbine Systems*, Antalya, Turkey, 2009.

Xing, Y., Spring, S., and Weigand, B., Experimental and Numerical Investigation of Heat Transfer Characteristics of Inline and Staggered Arrays of Impinging Jets, *J. Heat Transf.*, vol. **132**, no. 9, p. 092201, 2010.

Xing, Y., Spring, S., and Weigand, B., Experimental and Numerical Investigation of Impingement Heat Transfer on a Flat and Micro-Rib Roughened Plate with Different Crossflow Schemes, *Int. J. Therm. Sci.*, vol. **50**, no. 7, pp. 1293–1307, 2011.

Zeitoun, O. and Ali, M., Nanofluid Impingement Jet Heat Transfer, *Nanoscale Res. Lett.*, vol. **7**, pp. 1–14, 2012.

Zu, Y.Q., Yan, Y.Y., and Maltson, J.D., CFD Prediction for Multi-Jet Impingement Heat Transfer, in *Proc. of ASME Turbo Expo 2009: Power for Land, Sea, and Air, Vol. 3: Heat Transf., Parts A and B*, Orlando, FL, pp. 483–490, 2009.

Zuckerman, N. and Lior, N., Jet Impingement Heat Transfer: Physics, Correlations, and Numerical Modeling, *Adv. Heat Transf.*, vol. **39**, pp. 565–631, 2006.